Article

Palladium−Ceria Catalysts with Enhanced Alkaline Hydrogen Oxidation Activity for Anion Exchange Membrane Fuel Cells

Marco Bellini,[†] Maria V. Pagliaro,[†] Anna Lenarda,[‡] Paolo Fornasiero,*,[‡] Marcello Marelli,[§]
Claudio Evangelisti,[§] Massimo Innocenti,[¶] Qingying Jia,[∥] Sanjeev Mukerjee,[∥] Jasna Jankovic,[□]
Lianqin Wang,[■] John R. Varcoe,[■] Chethana B. Krishnamurthy,[△] Ilya Grinberg,[△] Elena Davydova,[#]
Dario R. Dekel,*,[#,▽] Hamish A. Miller,*,[†] and Francesco Vizza*,[†]

[†]Istituto di Chimica dei Composti Organometallici (CNR-ICCOM), Via Madonna del Piano 10, 50019, Sesto Fiorentino 50019, Italy

[‡]Department of Chemical and Pharmaceutical Sciences, INSTM, University of Trieste, Via L. Giorgieri 1, Trieste, 34127 Italy

[§]Istituto di Scienze e Tecnologie Molecolari (ISTM-CNR), via Camillo Golgi 19, 20133 Milano, Italy

[¶]Dipartimento di Chimica 'Ugo Schiff', Università degli Studi Firenze, Via della Lastruccia, 3-13, 50019 Sesto Fiorentino, Italy

[∥]Department of Chemistry and Chemical Biology, Northeastern University, Boston, Massachusetts 02115, United States

[□]Materials Science and Engineering Department, University of Connecticut, Storrs, Connecticut 06269, United States

[■]Department of Chemistry, University of Surrey, Guildford GU2 7XH, U.K.

[△]Department of Chemistry, Bar-Ilan University, Ramat Gan, 52900, Israel

[#]The Wolfson Department of Chemical Engineering, Technion—Israel Institute of Technology, Haifa, 3200003, Israel

[▽]The Nancy & Stephan Grand Technion Energy Program (GTEP), Technion—Israel Institute of Technology, Haifa 3200003, Israel

S *Supporting Information*

ABSTRACT: Anion exchange membrane fuel cells (AEMFCs) offer several important advantages with respect to proton exchange membrane fuel cells, including the possibility of avoiding the use of platinum catalysts to help overcome the high cost of fuel cell systems. Despite such potential benefits, the slow kinetics of the hydrogen oxidation reaction (HOR) in alkaline media and limitations in performance stability (because of the degradation of the anion conducting polymer electrolyte components) have generally impeded AEMFC development. Replacing Pt with an active but more sustainable HOR catalyst is a key objective. Herein, we report the synthesis of a Pd−CeO$_2$/C catalyst with engineered Pd-to-CeO$_2$ interfacial contact. The optimized Pd−CeO$_2$ interfacial contact affords an increased HOR activity leading to >1.4 W cm^{-2} peak power densities in AEMFC tests. This is the only Pt-free HOR catalyst yet reported that matches state-of-the-art AEMFC power performances (>1 W cm^{-2}). Density functional theory calculations suggest that the exceptional HOR activity is attributable to a weakening of the hydrogen binding energy through the interaction of Pd atoms with the oxygen atoms of CeO$_2$. This interaction is facilitated by a structure that consists of oxidized Pd atoms coordinated by four CeO$_2$ oxygen atoms, confirmed by X-ray absorption spectroscopy.

KEYWORDS: fuel cells, platinum free, anion exchange membrane, palladium, ceria
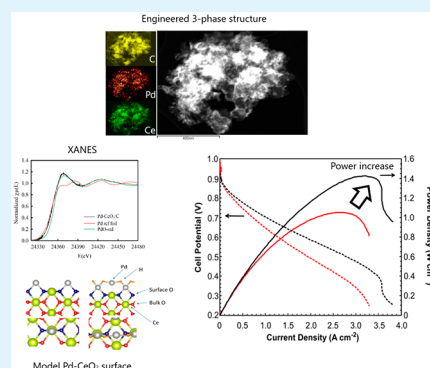
1. INTRODUCTION

It is well-known that the kinetics of the hydrogen oxidation reaction (HOR) in alkaline media is much slower than in acidic solutions.[1,2] A recent comprehensive review of the current understanding of HOR electrocatalysis in basic media highlights the challenges involved in developing new materials with high activity in this medium.[3] The large overpotential for the HOR at high pH,[3] combined with the low efficiency and poor stability of anion exchange membranes (AEMs),[4−8] are the two main obstacles to the development of high-performance anion exchange membrane fuel cells (AEMFCs).[9−11]

The HOR activity of carbon-supported noble metals (Pt, Pd, and Ir) decreases by around 2 orders of magnitude when transitioning from low to high pH.[12] Only recently have researchers approached the problem in a systematic manner with the purpose of elucidating the mechanisms and defining the activity descriptors for the HOR at high pH.[2,13−18] Most importantly, the role of OH* in the HOR process under

alkaline conditions is still unclear.[3] There are two possible mechanisms involving adsorbed hydrogen (H_{ad}) on the metal catalyst surface.[3] The first is that H_{ad} is initially desorbed as a proton (the mechanism that occurs in an acidic environment) which then reacts with OH^- to generate water (eqs 1 and 2). If this mechanism predominates at high pH, then the hydrogen binding energy (HBE) would be the sole determining factor for the HOR kinetics.

$$H_{ad} \rightarrow H^+ + e^- \tag{1}$$

$$H^+ + OH^- \rightarrow H_2O \tag{2}$$

The second mechanism includes OH^- that is also adsorbed on the surface of the metal catalyst ($M-OH_{ad}$), where the H_{ad} and OH_{ad} subsequently react to form water (eqs 3 and 4). With this mechanism, both HBE and the OHBE (OH_{ad} binding energy) would be important for determining the HOR activity.[3]

$$OH^- \rightarrow OH_{ad} + e^- \tag{3}$$

$$H_{ad} + OH_{ad} \rightarrow H_2O \tag{4}$$

A series of careful studies of both Pt and Pt alloy catalysts have led to the general consensus that the main descriptor for HOR activity on noble metals in base is the HBE.[12,19,20] A pair of important recent studies report the weakening of the $M-H_{ad}$ interaction to be the determining factor in the enhancement of the HOR with surface-controlled Pt-based nanoparticles of well-defined composition: first, with a PtRu/C catalyst[21] and, second, with both alloyed PtNi nanoparticles and acid-washed PtNi nanoparticles.[15] The authors concluded that the incorporation of a strongly OH binding component into the alloy was not beneficial in improving activity. Conversely, the introduction of a foreign atom in Pt alloys adjusts the electronic state of the Pt to tune the HBE and increase HOR activity.[15] Recent work by Lin Zhuang and co-workers confirms the HBE as the primary descriptor for the alkaline HOR on Pt. Improved activity at higher temperature is linked to a weaker hydrogen bond energy.[22]

The alternative bifunctional mechanism involving adsorbed OH groups was first investigated by Markovic and co-workers.[23] They demonstrated that the HOR rate can be improved by optimizing the balance between the active sites required for the adsorption and dissociation of H_2 (noble metal, for example, Pt or Pd) and the adsorption of hydroxyl species (OH_{ad}).[23] The conclusion was that a bifunctional catalyst with both H and OH adsorption sites is necessary to facilitate the HOR. To show this, the authors prepared a series of bimetallic catalysts with stronger OH adsorption characteristics and confirmed that this was beneficial for the HOR activity. More recent, experimental proof to support the bifunctional mechanism has been provided for Pt/C catalyst with surface doped Ru.[13] Additional information supporting the bifunctional mechanism has been provided in a recent review.[3] The presence of OH_{ad} species on the surface Ru sites in the HOR potential region and its promoting effect on the oxidation of H_{ad} was demonstrated thereby verifying the bifunctional mechanism for the HOR under alkaline conditions.

We have recently reported Pd NPs deposited on a mixed support of carbon and CeO_2, which show improved HOR activity at high pH.[24,25] When deployed in a Pt-free AEMFC, the Pd/C−CeO$_2$ catalyst in combination with a Ag-based cathode, achieved a peak power density of 0.5 W cm^{-2} (at 330 mV)[24] and more recently, combined with a PdCu/C cathode, a record power density of 1 W cm^{-2} (at 420 mV).[26] Despite fluctuations in the price difference between PGMs, Pd remains a more sustainable alternative to Pt, both in terms of natural abundance and recently reported low toxicity.[27] Importantly, it is the Pd to CeO_2 interaction that leads to increased HOR activity and has been confirmed for Pd−CeO$_2$ type materials prepared independently by different synthetic methods.[28] AEMFCs with high power densities can be realized through the combination of Pd−CeO$_2$ with PGM-free cathode catalysts for overall system cost reduction.

In this Article, we rationalize the enhancement in the HOR activity of Pd−CeO$_2$/C catalysts and show that the HOR activity is directly related to the Pd−CeO$_2$ interfacial structure. The HOR activity is consequently improved by engineering the Pd−CeO$_2$ interface. A reproducible and scalable synthesis is reported that consists of the addition of CeO_2 to carbon using an organometallic precursor followed by Pd deposition. The resulting Pd−CeO$_2$ interfacial structure obtained is confirmed by multiple electron microscopies with associated elemental maps produced by energy dispersive X-ray spectroscopy. More than 1.4 W cm^{-2} peak power density in H_2/O_2 AEMFC testing is demonstrated. Furthermore, density functional theory (DFT) calculations confirm that the H atom adsorbs less strongly on a Pd−CeO$_2$ surface than that of Pd(111), suggesting that the Pd−CeO$_2$ structure deactivates H adsorption and hence promotes the catalytic HOR.

2. EXPERIMENTAL SECTION

All material manipulations during materials preparation, except as stated otherwise, were routinely performed under a N_2 atmosphere using standard airless techniques. Carbon black (Vulcan XC-72 pellets) was purchased from Cabot Corp., USA. All metal salts and reagents were purchased from Aldrich and used as received. All the solutions were freshly prepared with doubly distilled deionized water. The benchmark Pd/C and Pd−CeO$_2$ reference catalysts (both 10% wt. Pd) were prepared as described in our previous publications.[24,25]

2.1. Synthesis of CeO$_2$/C. The CeO_2/C material was prepared as follows. In a typical synthesis, first 300 mg carbon black was treated for 3 h in 200 mL of a HNO_3 solution (4.0 M) to functionalize the carbon surface with oxygen bearing groups. This material was then dispersed in ethanol by sonication for 30 min and a THF solution of cerium(IV) tetrakis(decyloxide) ($Ce(C_{10}H_{21}O)_4$, freshly prepared with a procedure reported elsewhere)[29] was added dropwise to obtain a final CeO_2 loading of 45% wt. After 30 min of sonication, 20 mL of a 10% vol. solution of H_2O in ethanol was added dropwise to hydrolyze the alkoxide and form the C-supported amorphous CeO_2, which was then further sonicated for 30 min. The solid product was collected by filtration through a 0.45 μm PTFE filter and washed thoroughly with ethanol. The solid material thus obtained was dried to constant weight.

2.2. Synthesis of Pd−CeO$_2$/C. The CeO_2/C support material (500 mg) was suspended in 100 mL of water by vigorous stirring for 1 h followed by sonication for 30 min. A solution of K_2PdCl_4 (0.17 g) in 20 mL of water was added (1 mL min^{-1}) under stirring, followed by continued stirring for 1 h. To this solution, aqueous KOH (2.5 M, 2.0 mL) was added followed by addition of ethanol (15 mL, added at 1 mL min^{-1}). The mixture was then heated at 80 °C for 1 h. After cooling to room temperature, the solid product was collected by filtration, washed with water until neutral and then dried to constant weight at 60 °C in air (Yield = 480 mg). The %wt. ratio of the three components in the catalyst Pd:CeO$_2$:C were 1:4:5 respectively (confirmed by TGA, Figure S1).

2.3. Electron Microscopy. Samples for the microscopy characterization were finely ground in an agate mortar, suspended in

isopropanol, and sonicated, and then, each suspension was dropped onto a holey carbon-coated copper grid (300 mesh) and dried overnight. Transmission electron microscopy (TEM) studies were performed on two instruments: (1) a ZEISS LIBRA200FE microscope equipped with a 200 kV FEG source and energy-dispersive X-ray spectra (EDS, Oxford INCA Energy TEM 200) and (2) a FEI TEM Osiris microscope with an accelerating beam voltage of 200 kV and ChemiSTEM EDS detector system, which was utilized for STEM/EDS analysis. Elemental maps were collected along with HAADF-STEM (high angular annular dark field scanning transmission electron microscopy) micrographs.

2.4. Ex Situ X-ray Absorption Spectroscopy (XAS). Measurements were carried out at the Pd L_3-edge in the transmission mode at the beamline 8-ID at the NSLS-II, Brookhaven National Laboratory, USA. The data were processed and fitted using the IFEFFIT-based Athena[30] and Artemis[31] programs. Scans were calibrated, aligned and normalized with background removed using the IFEFFIT suite[32] (version 1.2.9, IFEFFIT Copyright 2005, Matthew Newville, University of Chicago, http://cars9.uchicago.edu/ifeffit/). The $\chi(R)$ were modeled using single scattering paths calculated by FEFF6.[33]

2.5. X-ray Powder Diffraction (XRD). Spectra were acquired at room temperature with a PAN analytical X'PERT PRO diffractometer, employing CuKα radiation (λ = 1.54187 Å) and a parabolic MPD-mirror. The spectra were acquired at room temperature in the 2Θ range from 5.0 to 120.0°, using a continuous scan mode with an acquisition step size of 0.0263° and a counting time of 49.5 s. Spectra are shown in the 2Θ range of 15−90°.

2.6. H₂ Temperature-Programmed Desorption (H$_2$-TPD). Analysis of second generation Pd−CeO$_2$/C and Pd/C was obtained using an AutoChem 2920 (Micromeritics) operated in the flowing mode. Thermal conductivity detector (TCD) was used to determine the H$_2$ concentration. The samples (0.1−0.2 g) were placed in the quartz reactor, adsorbed water was removed by heat treating the samples at 200 °C for 30 min. H$_2$ adsorption was carried out at 60 °C using a mixture of 10 vol % H$_2$/Ar at a flow rate of 50 mL min^{-1}. Afterward, the gas mixture was switched to Ar with a flow rate of 50 mL min^{-1} until obtaining the baseline of TCD signal. Thermal desorption traces were recorded at the temperature ramp of 10, 20, and 30 deg min^{-1} up to 500 °C. The resultant curves were deconvoluted using skewed log-normal distribution.

2.7. Cyclic Voltammetry (CV). Measurements were performed with a Princeton 2273A potentiostat/galvanostat, using a three-electrode arrangement with an Ag/AgCl reference electrode and a platinum foil counter electrode (25 × 25 × 0.1 mm³). No IR drop compensation was applied to any of the performed experiments. The potential scale of the CV curves was then converted to the reversible hydrogen electrode (RHE) scale. A portion (1−2 mg) of each catalyst was introduced into a 5 mL glass vial together with a 50:50 water/ethanol (99.8%, Fluka) solution to obtain a 2.5 mg mL^{-1} dispersion, and 1%wt. of Nafion 117 solution. The resulting suspension was sonicated for 30 min. The metal loading on each electrode was determined by weighing the amount of the deposited ink onto the glassy carbon electrode.

2.8. Hydrogen Pump Experiments. Tests were carried out using 5 cm² HOR catalyst coated carbon cloth electrodes as anode combined with an anion exchange membrane (AEM) and a Pt/C cathode electrode for the hydrogen evolution reaction (HER). As HOR catalyst, Pt/C (40 wt %, 0.44 mg$_{Pt}$ cm^{-2} + 60 wt % AS4 ionomer in catalyst layer) was compared to the various Pd based materials discussed in this article. Electrodes were prepared by spreading an ink suspension composed of water, 1-propanol, catalyst, and AS4 ionomer solution (Tokuyama corp., Japan) onto carbon cloth supports using a Mayer rod to control the catalyst loading. Prior to use, the AEM (A201, Tokuyama corp., Japan) was hydrated and ion exchanged for 2 h in 1 M KOH. The membrane electrode assemblies were prepared by mechanically pressing the anode, cathode, and the membrane within the cell testing hardware (Scribner Associates USA). A cell operating temperature of 60 °C with 100% relative humidity hydrogen/oxygen gases was used. During cell heating and humidification, N$_2$ was flowed over the HER electrode

and H$_2$ through the HOR electrode (both at 100 mL min^{-1}). Cell stabilization was achieved by slowly ramping from 10 to 100 mA cm^{-2} (20 mA cm^{-2} increments, 1 min per step), followed by a 30 min hold at 100 mA cm^{-2}. Polarization curves were taken from 50 to 400 mA cm^{-2} in 40 mA cm^{-2} increments, followed by a 1 h constant current test at 300 mA cm^{-2}.

2.9. Fuel Cell Testing. *MEA Preparation.* The catalyst deposited on gas diffusion electrode (GDE) method for preparing AEMFC electrodes was described in previous publications.[34−36] Prior to preparation of the catalyst ink, a previously benzyltrimethylammonium grafted ETFE-based AEI powder with an IEC = 1.26 ± 0.06 mmol g^{-1} was ground with a pestle and mortar for 10 min. The AEI powder used in previous studies and was synthesized via the radiation-grafting of vinylbenzyl chloride onto an ETFE powder (Fluon Z8820X, supplied by AGC Europe) with subsequent amination using trimethylamine. For each cathode GDE, Pt/C (Alfa Aesar, Johnson Matthey HiSpec 4000, 40 wt % Pt) and AEI powder (20% wt. of the total solid mass) were mixed together with 1 mL water and 9 mL 2-propanol. The cathode catalyst ink was then homogenized with ultrasound for 30 min, sprayed onto a Toray TGP-H-60 carbon paper gas diffusion substrate (Alfa Aesar, nonteflonated), and dried in air. For the anode GDEs, the Pd−CeO$_2$/C was used as catalyst (with 20 wt % AEI). The 5 cm² GDEs were loaded with 0.30 ± 0.02 mg$_{Pd}$ cm^{-2} and 0.40 ± 0.02 mg$_{Pt}$ cm^{-2} for anode and cathode electrodes, respectively.

All electrodes and AEMs (made from radiation-grafting 15 μM LDPE with vinylbenzyl chloride, followed by amination with TMA, ion-exchange capacity (IEC) = 2.54 mmol g^{-1})[37] were immersed in aqueous KOH solution (1 M) for 1 h and then washed thoroughly in water (to remove excess KOH) before assembly into a 5 cm² fuel cell fixture (Scribner Associates, USA) using 5 N m torque.

2.10. Fuel Cell Performance Data Collection. An 850e fuel cell test station (Scribner Associates, USA) was used for testing. The fuel cell temperature was kept at 80 °C. H$_2$ and O$_2$ gas feeds with flow rates of 1 and 2 L min^{-1} (SLPM) were supplied to the anode and cathode, respectively, with no back-pressurization. The dew-point for both anode and cathode gas supplies was 76 °C (calculated relative humidity, RH, of 65%). All followers (heated lines between the fuel cell tester and the fuel cell fixture) were set at the same temperatures as the gas dew points. The MEAs were activated by discharging the cell at a constant voltage of 0.5 V during cell heating, until a steady current density was observed. Beginning-of-life AEMFC performance data were collected under controlled galvanostatic discharge steps where data (at each current density) were recorded after potentials had stabilized. The internal ohmic resistances were estimated using the 850e instrument's internal current interrupt method.

2.11. Density Functional Theory (DFT). Calculations were performed with all electron full potential method implemented in the Fritz-Haber-Institute ab initio molecular simulations (FHI-aims) package.[38] The atomic zero-order regular approximation (ZORA) was used to treat relativistic effects for all the atoms in the system.[39] We used the "tight" settings for integration grids and the exchange-correlation energy was evaluated with the PBE functional.[40] The convergence criteria for the energy and force were set to 10−6 eV and 10−4 eV Å^{-1}, respectively. Gaussian smearing with the width of 0.1 eV was used to speed up the convergence of the states near the Fermi level.

CeO$_2$ (110) surface model was used in this work, consisting of five atomic layers and has a vacuum gap of 10 Å perpendicular to the surface. Monkhorst−Pack Brillouin zone sampling was used with a 13 × 13 × 1 grid. During the geometry optimization, all the atoms are allowed to relax.

The adsorption energy E_{ad} is defined as

$$E_{ads} = (E_{surface+adsorbate}) - (E_{surface} + E_{adsorbate})$$

where $E_{surface}$ and $E_{adsorbate}$ are the energies of the bare surface and the free adsorbate in the gas phase, respectively, and $E_{surface+adsorbate}$ is the total energy of the interacting surface and the adsorbate. According to this equation, a more negative E_{ad} value corresponds to stronger

adsorption. The HBE is calculated relative to H_2 in the gas phase and is given by

$$HBE = E_{surface+adsorbate} - E_{surface} - 0.5E_{H_2}$$

where E_{H_2} is the energy of the gas-phase hydrogen molecule. The differential adsorption free energy is given by using the equation reported by Nørskov and co-workers.[41]

3. RESULTS AND DISCUSSION

3.1. Catalyst Characterization. An engineered nano-structure that optimizes the active two-phase contact between the Pd and CeO_2 phases has been achieved. An organometallic cerium precursor (cerium(IV) tetrakis(decyloxide) (Ce-$(C_{10}H_{21}O)_4$) is used to coat the carbon support particles with a highly homogeneous nanothin layer of nanostructured CeO_2 (transition electron microscopy (TEM) and high angular annular dark field scanning transmission electron microscopy (HAADF-STEM) images are shown in Figure 1).
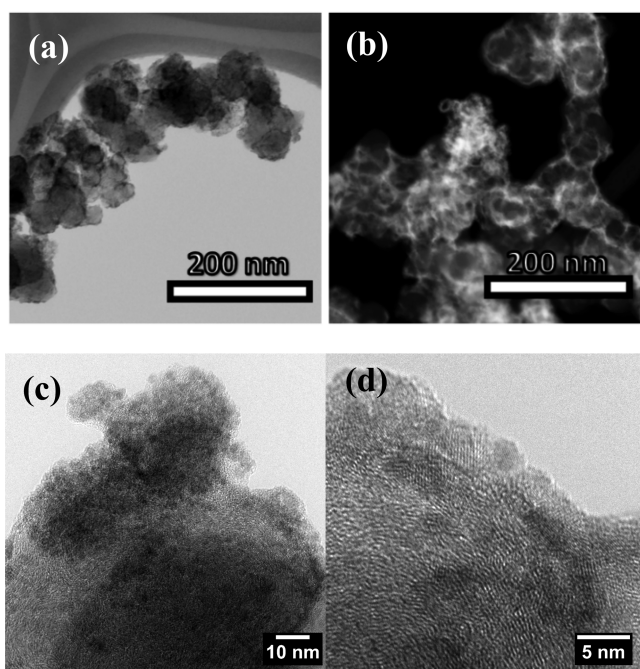
Figure 1. Representative (a) TEM, (b) (HAADF) STEM, (c and d) HR-TEM images of Pd−CeO_2/C.

High-resolution images show the presence of crystalline nanodomains ranging from 2 to 3 nm in size. Lattice fringe analysis revealed a *d*-spacing of 3.15 Å, characteristic of (111) planes of cubic CeO_2. After the addition of Pd, individual nanoparticles are not detected even using high-resolution TEM due to a high dispersion within the CeO_2 phase. On the other hand, Pd nanoparticles were not detected even using high resolution TEM or STEM at high magnification due to the possible formation of small Pd clusters or isolated Pd atoms embedded in the CeO_2 matrix (see X-ray absorption spectroscopy results discussed below). Analysis by HAADF-STEM-EDS (energy-dispersive X-ray spectroscopy) mapping demonstrates the homogeneous distribution of all three components (CeO_2, Pd, and C) throughout the catalyst (see also Figures S2−S4). The images and EDS element maps in Figure 2 show finely dispersed Pd and CeO_2 on the surface of Vulcan carbon support. A semiquantitative analysis resulting
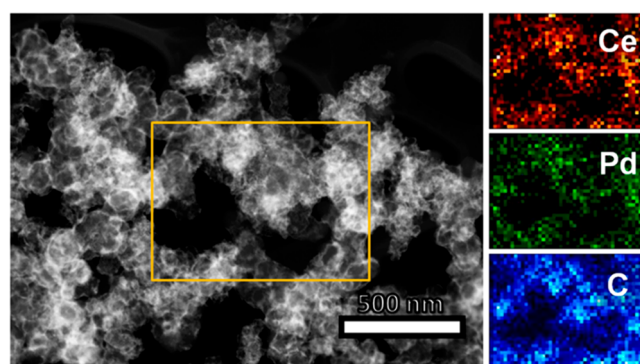
Figure 2. STEM images of Pd−CeO_2/C: HAADF image and STEM-EDS mapping of the selected area showing the CeO_2 (red), Pd (green), and carbon (blue) elemental maps.

from the EDS spectrum reveals a surface Pd to CeO_2 ratio of 1:2.3.

The X-ray powder diffraction (XRD) patterns of CeO_2/C and Pd−CeO_2/C are compared in Figure 3. Both patterns are
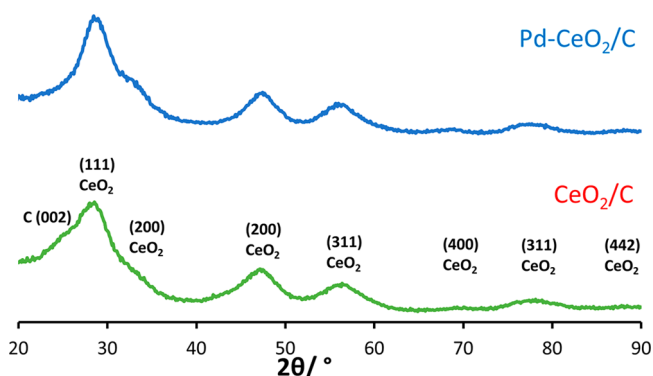
Figure 3. XRD patterns of CeO_2/C and Pd−CeO_2/C.

dominated by the reflections originated by the cubic structure of CeO_2; the line broadening of the reflections is consistent with the formation of small nanosized particles of CeO_2. The signal representative of metallic Pd(0) at $2\theta = 40°$ Pd(111) is not visible in the pattern of Pd−CeO_2/C, indicating non-crystalline, highly oxidized, and small nature of the palladium structures in this catalyst.

The electronic state and local coordination environment of Pd was probed by combining X-ray absorption near edge structure (XANES) and the Fourier transform (FT) of the extended X-ray absorption fine structure (FT-EXAFS) of the spectra collected at the Pd L_3-edge (Figure 4). These spectra are compared together with the XANES and FT-EXAFS of a Pd reference metallic foil for comparison. The prominent white line intensity of the XANES is comparable to that of a PdO standard (Figure 4a) and clearly indicates that the Pd in Pd−CeO_2/C is highly oxidized. This is further confirmed by the prominent Pd−O peak around 1.5 Å (without phase correction). The small peak at around 2.5 Å implicates the existence of some metallic Pd, either a very small amount or very small clusters, which is further supported by a reasonable EXAFS fitting excluding the Pd−Pd scattering path (Figure 4b). The EXAFS fitting shows that on average Pd is surrounded by 3.9 oxygen atoms in the first shell with a typical bond distance of 2.0 Å (Table 1). These XAS results together depict a single Pd atom embedded in CeO_2 as the
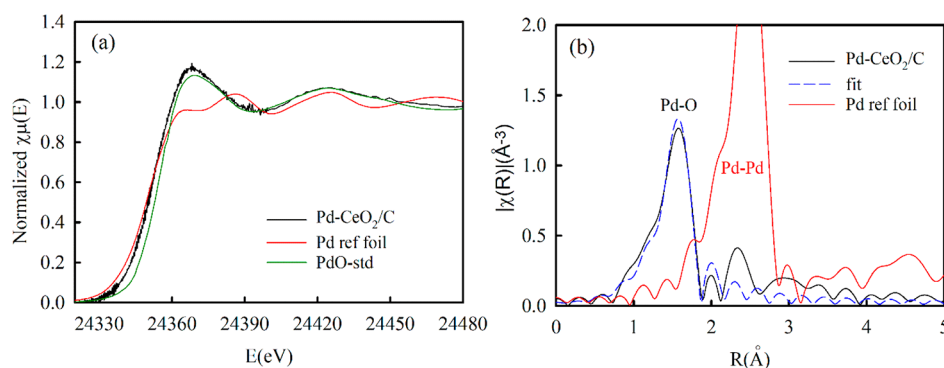
Figure 4. (a) XANES and (b) FT-EXAFS spectra at the Pd L_3-edge of a Pd reference foil and Pd−CeO$_2$/C with curve fitting.

Table 1. Summary of EXAFS Results for Pd−CeO$_2$/C^a

scattering path	edge (eV)	bond length (Å)	coordination number	D−W factor (Å^2)
Pd−O	3.9 ± 1.8	2.00 ± 0.01	3.9 ± 0.4	0.002 ± 0.001

$^a S_0^2$ fixed at 0.62 as obtained by fitting the reference foil. Fits were done in R-space, $k^{1,2,3}$ weighting at the Pt L_3-edge with the windows of 1.0 < R < 2.4 Å and Δk = 2.93−12.86 Å^{-1}. Statistical errors of the least-squares fits were determined by ARTEMIS.

dominant structure in the Pd−CeO$_2$/C catalyst, wherein the Pd is in contact with the oxygen from CeO$_2$ rather than Ce. The distribution of ceria over the carbon support in Pd−CeO$_2$/C is homogeneous and the Pd when incorporated interacts solely with CeO$_2$. Such an optimized structure with the direct Pd−O interfacial interaction in this new material results in a greatly enhanced HOR activity as favorable electronic interactions are maximized, including the weakening of the Pd−H interaction, as demonstrated through H$_2$-temperature-programmed desorption (TPD) analyses and DFT calculations discussed below.

The XAS/XRD studies confirm that the unique structure of Pd−CeO$_2$/C results in an unusually highly oxidized Pd closely coordinated to the oxygen atoms of CeO$_2$. The way that this structure enhances the HOR activity can be elucidated by investigating H$_2$ adsorption/desorption characteristics. Pd−CeO$_2$/C was studied using TPD analysis and the results compared with those obtained with a Pd/C catalyst with the

same metal loading. H$_2$-TPD spectra (Figure 5) show distinguishable low temperature (<200 °C) and high temperature (>200 °C) hydrogen desorption peaks which were deconvoluted for both the Pd/C and Pd−CeO$_2$/C catalysts.

The mass specific amount of H$_2$ desorbed from Pd−CeO$_2$/C (0.57 mmol g$_{cat}^{-1}$) is higher than that measured for Pd/C (0.42 mmol g$_{cat}^{-1}$). The ratio of the hydrogen desorbed at temperatures below 200 °C is also much higher for Pd−CeO$_2$/C (9.9%) than for Pd/C (1.6%). The desorption peaks I and II appear on Pd−CeO$_2$/C spectra at higher temperature values than for Pd/C. The opposite thermal shift is observed for the peaks III, IV and V: the maximum desorption rate temperature values are higher for Pd/C. The peak of highest intensity on Pd/C is observed at 292 °C (peak III), while Pd−CeO$_2$/C is mainly populated by the hydrogen desorbing at 312 °C (peak IV). Full analysis of the experimental data at three different temperature ramp values are presented in the Figures S5−S10.

Below a critical temperature of 298 °C in Pd−H binary systems, two phases can coexist: a solid solution of H in Pd (α-phase) and the Pd hydride (β-phase).[42] It is known that, at room temperature, Pd can absorb H$_2$ to form Pd hydride at a H$_2$ partial pressure exceeding 0.013 atm (at lower partial pressures H$_2$ dissolves only sparingly to form the α-phase). Over the temperature range of 50−100 °C, decomposition of Pd hydride species from supported Pd catalysts has been previously reported.[43] Thus, on the basis of the literature data,[44] the desorption peaks I and II at temperatures below
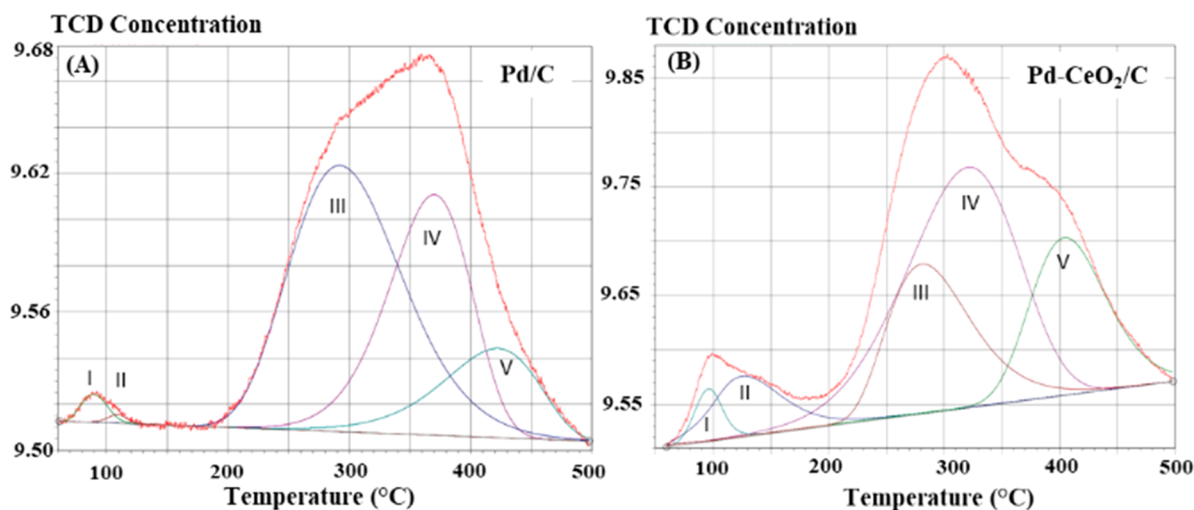

Figure 5. Deconvolution of H$_2$-TPD spectra for (A) Pd/C and (B) Pd−CeO$_2$/C catalysts. Temperature ramp = 10° min^{-1}.

Table 2. Comparison of H_2-TPD data for Pd/C and Pd−CeO$_2$/C

| | 10% Pd/C | | | | 10% Pd−CeO$_2$/C | | | |
peak	t (°C)	mmol(H_2)/g$_{cat}$	ratio	H/Pd[a]	t (°C)	mmol(H_2)/g$_{cat}$	ratio	H/Pd
I	91.5	0.00706	0.016	0.015	95.8	0.00954	0.016	0.020
II					121.7	0.04747	0.083	0.101
∑I+II		0.00706	0.016	0.015		0.05701	0.099	0.121
III	292.0	0.20307	0.470	0.432	275.9	0.06447	0.113	0.138
IV	370.3	0.12546	0.290	0.267	313.8	0.30893	0.537	0.658
V	411.5	0.09641	0.284	0.205	405.8	0.08673	0.151	0.185
∑III+IV+V		0.42494	0.984	0.904		0.46039	0.801	0.980
∑		0.42494	1.00	0.919		0.57441	1.00	1.223

[a]Number of H atoms per one Pd atom.
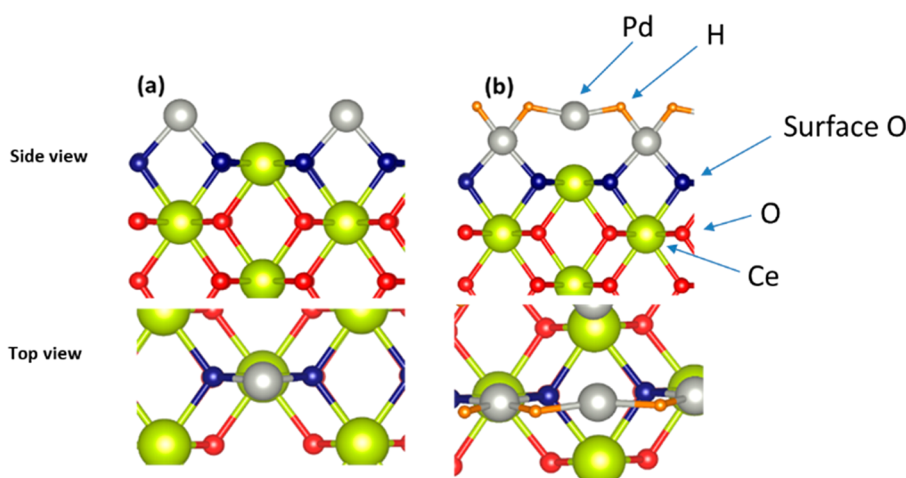
Figure 6. (a) Adsorption of Pd on bridge site between the O atoms of the CeO$_2$ (110) (b) Adsorption of H in between the Pd atoms. Green, gray, and orange balls represents Ce, Pd, and H atoms, respectively. O atoms are shown in red and blue to distinguish the surface O atoms (blue) from other O atoms (red) in the slab.

150 °C (Figure 5) can be attributed to β-phase decomposition. In this region, the amount of H atoms per Pd atom (H/Pd ratio data in Table 2) for Pd/C is 0.015 and is almost 1 order of magnitude lower than that for the Pd/C−CeO$_2$. Comparison of H$_2$-TPD data with the DFT calculations (see below) allow us to assume that the higher affinity of Pd−CeO$_2$/C to hydrogen dissolution might result in its lower affinity to hydrogen chemisorption. The assumption is in good agreement with earlier reported results showing that H binds less strongly to Pd hydride than to Pd.[45] The higher temperature peaks III, IV, and V can be assigned to strong adsorption of hydrogen, mostly to the spillover, transport, and storage of chemisorbed H atoms on the supporting CeO$_2$ material.[46,47] The overall ratio of H/Pd (Table 2) for Pd/C catalyst is 0.92, compared to 1.22 for the Pd−CeO$_2$/C. The higher adsorption of H$_2$ in Pd−CeO$_2$/C can hence be assigned to the well-known H$_2$ spillover capacity of CeO$_2$.[48−50] By comparison, values of H/Pd reported in literature for Pd/C catalysts lie within a large range of 0.005−0.77.[51]

3.2. DFT Calculations. The CeO$_2$−Pd system was modeled by the deposition of Pd atoms on the top of the CeO$_2$ (110) surface. We investigated different possible adsorption sites for the Pd binding on the CeO$_2$ (110) surface and found that Pd prefers to be in the bridge position between the O atoms of the CeO$_2$ (Figure 6a), which is consistent with previous reports.[52,53] We calculated the HBE of Pd−CeO$_2$ as compared to Pd. This has been described as one possible descriptor for the HOR and has been investigated for other

systems using DFT calculations.[54,55] We found that H prefers to adsorb in the bridge site between the Pd atoms, as shown in Figure 6b, and the HBE (relative to the gas phase H$_2$) changes from −0.80 eV for Pd(111) to −0.46 eV for the Pd−CeO$_2$ surface (Tables 3 and S3). Since the HBE of the Pd metal is

Table 3. H Binding Energy on Pd−CeO$_2$ Substrate[a]

| structure	E_{ad}	HBE (1/2 H$_2$ as ref)	external potential (U) = 0 V (1/2 H$_2$)
Pd(111)	−4.14	−0.80	−1.03
Pd−CeO$_2$	−3.80	−0.46	−0.67
2 layer Pd on CeO$_2$	−4.05	−0.71	−0.94
3 layer Pd on CeO$_2$	−4.03	−0.70	−0.93

[a]The HBE is in electronvolts per H atom.

located on the left side of the volcano curve of HOR activity, the HOR activity is expected to be enhanced by a slight shift of the HBE to higher (more positive) values. Therefore, the weaker H adsorption strength on Pd−CeO$_2$ is consistent with our experimental observations of higher HOR activity.

The variation of HBE with the number of Pd layers on CeO$_2$ (110) surface was also investigated. Our calculations show that one monolayer (ML) of Pd on CeO$_2$ is catalytically more active for HOR than with multiple layers of Pd (Table 3). The significant direct metal−substrate interaction between the first layer of Pd atoms and O atoms of CeO$_2$ surface deactivates the
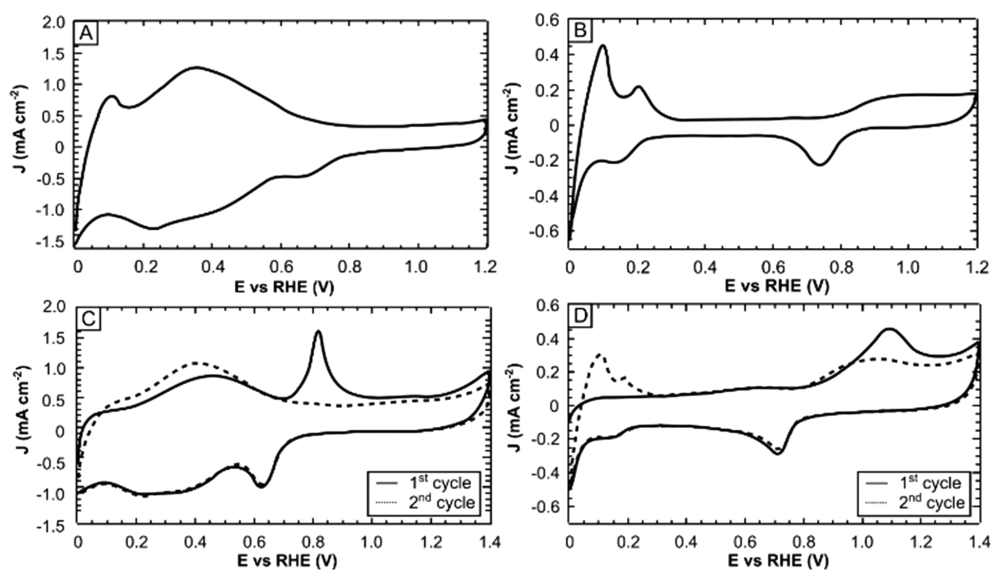
Figure 7. Cyclic voltammetry of Pd−CeO$_2$/C in static N$_2$-saturated aqueous solutions of (A) KOH (0.1 M) and (B) HClO$_4$ (0.2 M) (50 mV s^{-1}). CO stripping voltammetry in aqueous solutions of (C) KOH (2 M) and (D) in HClO$_4$ (0.2 M) (20 mV s^{-1}).
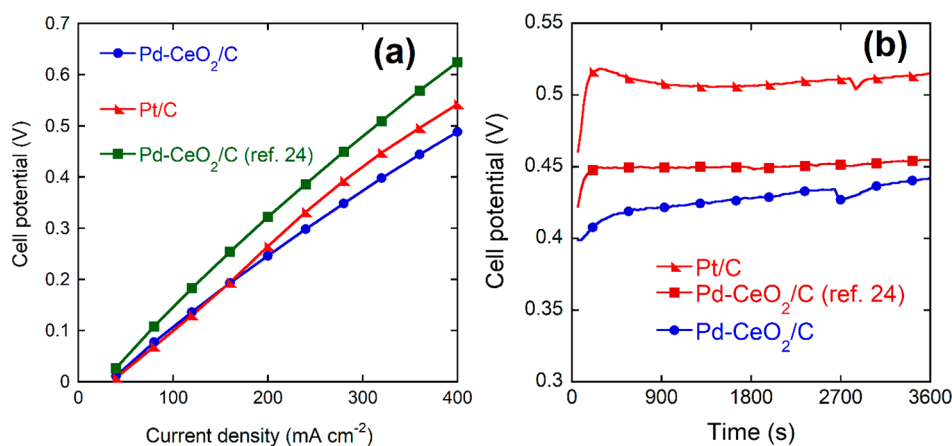
Figure 8. (a) Polarization curves of H$_2$ pumping tests (anode loadings: Pt/C = 0.45 mg cm^{-2} and Pd−CeO$_2$/C = 0.2 mg cm^{-2}) and (b) cell performance at a constant current density of 300 mA cm^{-2} for 1 h (T_{cell} = 60 °C, anode H$_2$ and cathode N$_2$ flow rates both 0.1 L min^{-1}, cathode electrode Pt/C = 0.45 mg cm^{-2}).

H-bond strength, whereas the second and third layers of Pd lack this direct metal−substrate interaction. As a result, the system almost behaves like bulk Pd, which leads to stronger binding. Nevertheless, even for two and three layers, the HBE is slightly deactivated compared to Pd(111), suggesting that the HOR activity will be enhanced in this case as well. This also suggests that very small particles or single atoms of Pd will produce higher HOR activity. The XAS data demonstrates that the Pd in the Pd−CeO$_2$/C catalyst exists in such a structure. In addition, this structure results in enhanced activity for the HOR under alkaline conditions as demonstrated in the electrochemical studies that follow.

3.3. Electrochemical Characterization. The synthesis of Pd−CeO$_2$/C was repeated five times on a 0.5 g scale to confirm repeatability. Tafel analysis was undertaken for each sample (Figure S11). The average values of Tafel slope and exchange current densities are 70 mV dec^{-1} and 20 A g$_{Pd}^{-1}$, respectively. Cyclic voltammetry (CV) in N$_2$ saturated aqueous KOH (0.1 M) shows Pd centered redox transitions that are broadened (usually well-defined under these conditions) with a much higher capacitive current density (Figure 7A).

Additionally, there is a large contribution from CeO$_2$ centered transitions in the H$_{UPD}$ zone in alkaline conditions, which are absent in acid media (Figure 7B). CO stripping voltammetry was undertaken in both alkaline (Figure 7C) and acidic (Figure 7D) conditions. The charge associated with the CO stripping peak was used to determine a value for the electrochemically active surface area (ECSA) of 63 m^2 g$_{Pd}^{-1}$.

H$_2$ pump electrochemical tests were used to evaluate and compare the HOR activity of Pd−CeO$_2$/C to reference catalysts in a simulated fuel cell environment. The catalyst was compared to commercial 40% wt. Pt/C (Alfa Aesar) and the Pd−CeO$_2$ catalyst previously reported.[24,25] The membrane electrode assemblies (MEAs) were formed by pressing together the anode and cathode to the commercial AEM within the cell hardware (no prior hot pressing). The MEAs were tested using polarization curves at 60 °C with humidified gases at both electrodes. The details of each catalyst studied and important data are listed in Table S2. The polarization curves (Figure 8a) show that the activity of Pd−CeO$_2$/C (in a fuel cell relevant MEA) outperforms a Pt/C anode even with half the metal loading (0.2 vs 0.4 mg$_{PGM}$ cm^{-2}). This is

corroborated using constant current density (300 mA cm^{-2}) load tests with each catalyst (Figure 8b).

3.4. AEMFC Testing. We performed AEMFC testing to evaluate the HOR activity of the Pd−CeO$_2$/C catalyst under fuel cell conditions. A benzyltrimethylammonium radiation grafted LDPE (low density polyethylene) AEM was used (30 μm hydrated, IEC = 2.54 mmol g^{-1}), as this class of membrane has excellent properties (conductivity, water back diffusion kinetics) and has been well proven in high-performance AEMFCs.[34−37,56−58] Cell conditions and all materials were kept constant including the cathode electrode and AEM with the exception of the anode catalyst. Two anode electrodes with the same catalyst and metal loading were prepared with (a) Pd−CeO$_2$/C and (b) the previously reported Pd−CeO$_2$ catalyst[24] (the latter as a reference material). The Pd loading was kept constant (0.25 mg$_{Pd}$ cm^{-2}). Significantly higher power densities were obtained (Figure 9) with the nano-
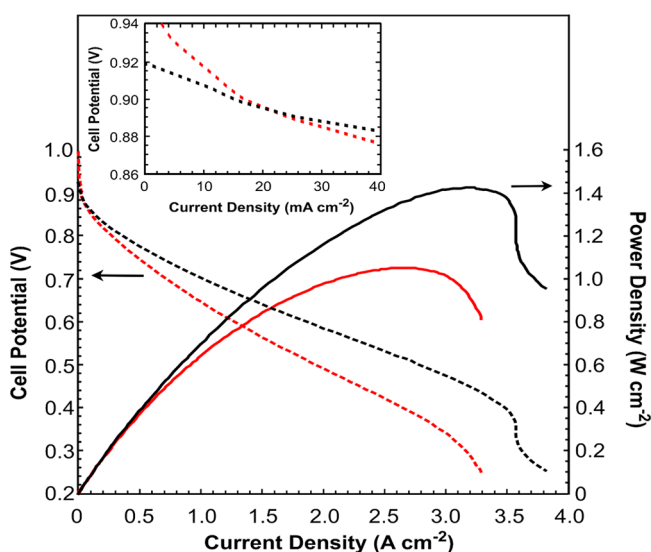
Figure 9. H$_2$/O$_2$ AEMFC performance data with Pd−CeO$_2$/C anode catalysts (0.25 mg$_{Pd}$ cm^{-2} loading), and a 40% wt. Pt/C cathode (0.4 mg cm^{-2} Pt loading): The Pd−CeO$_2$/C described in this work (black curves) and a reference catalyst (red curves).[24] Both electrodes contain 20% wt. of radiation-grafted ETFE-based anion-exchange ionomer (AEI) powder ionomer. H$_2$ was provided to the anode at 1.0 L min^{-1}. O$_2$ was fed to the cathode at 2.0 L min^{-1}. The cell temperature was 80 °C and anode/cathode dew-points were both 76 °C (no back-pressurization).

structured Pd−CeO$_2$/C catalyst. Within the initial activation (electrokinetic) region (see Figure 9 insert) this catalyst has higher activity at all potentials below 0.9 V. Interestingly, the ohmic and mass transport losses are also significantly reduced. This must all be attributable to the new improved Pd−CeO$_2$ interface obtained through the new synthesis procedure as all other aspects (materials, loadings, and cell test conditions) were fixed. The internal ohmic resistance was monitored during testing and shows also an improved conductivity of the Pd−CeO$_2$/C MEA (see Figure S12). Hence, the new catalyst also enables an enhanced catalyst-ionomer dispersion within the electrode layer leading to higher ionic conductivity for passage of the OH$^-$ anions. Under the same gas feeding conditions, the enhanced activity (current densities above 3.5 A cm^{-2}) results in the appearance of larger mass transfer losses,

clearly seen in the curve for Pd−CeO$_2$/C that we believe is due to anode flooding phenomena.

4. CONCLUSIONS

This study demonstrates that Pt-free hydrogen oxidation reaction electrocatalysts can be developed for high power density anion-exchange membrane fuel cells. A key aspect of this challenge is overcoming the poor activity of HOR catalysts in alkaline media. In doing this, we must also seek to gain clearer understanding of the nature of the activity descriptors for HOR catalysts in alkali in which there remains some debate. Having shown that certain Pd−CeO$_2$ interactions enhance the HOR activity of Pd in alkali, we have endeavored to describe the origin of this activity enhancement as well as engineer the catalyst structure and synthesis procedure to maximize the performance of this new class of fuel cell electrocatalyst. The preparation method, involving an organo-metallic cerium-based precursor, allowed us to obtain an optimized Pd−CeO$_2$ contact on the nanoscale. XAS investigations confirm this structure and DFT calculations have shown how Pd in this structure has a weakened interaction with adsorbed H. At the same time, the H$_2$ spillover capacity of CeO$_2$ in the catalyst facilitates the adsorption of more H$_2$ per Pd. The enhanced HOR activity of this Pd−CeO$_2$/C catalyst allowed us to obtain 1.4 W cm^{-2} of peak power density in H$_2$/O$_2$ AEMFC testing (a new record for a non-Pt anode catalyst).

■ ASSOCIATED CONTENT

Ⓢ Supporting Information

The Supporting Information is available free of charge on the ACS Publications website at DOI: 10.1021/acsaem.9b00657.

> Detailed material characterization; TGA, HAADF-STEM, EDS mapping, electron tomography, and H$_2$TPD curves; and electrochemical data Tafel curves, H$_2$-pump data, and fuel cell ohmic resistance measurements (PDF)

■ AUTHOR INFORMATION

Corresponding Authors
*E-mail: hamish.miller@iccom.cnr.it.
*E-mail: francesco.vizza@iccom.cnr.it.
*E-mail: pfornasiero@units.it.
*E-mail: dario@technion.ac.il.

ORCID Ⓞ
Paolo Fornasiero: 0000-0003-1082-9157
Claudio Evangelisti: 0000-0002-8855-2592
Chethana B. Krishnamurthy: 0000-0002-7615-5688
Dario R. Dekel: 0000-0002-8610-0808
Hamish A. Miller: 0000-0003-1668-6476

Notes
The authors declare no competing financial interest.

■ REFERENCES

(1) Elbert, K.; Hu, J.; Ma, Z.; Zhang, Y.; Chen, G. Y.; An, W.; Liu, P.; Isaacs, H. S.; Adzic, R. R.; Wang, J. X. Elucidating Hydrogen Oxidation/Evolution Kinetics in Base and Acid by Enhanced Activities at the Optimized Pt Shell Thickness on the Ru Core. *ACS Catal.* **2015**, *5* (11), 6764−6772.

(2) Ramaswamy, N.; Ghoshal, S.; Bates, M. K.; Jia, Q. Y.; Li, J. K.; Mukerjee, S. Hydrogen oxidation reaction in alkaline media: Relationship between electrocatalysis and electrochemical double-layer structure. *Nano Energy* **2017**, *41*, 765−771.

(3) Davydova, E. S.; Mukerjee, S.; Jaouen, F.; Dekel, D. R. Electrocatalysts for Hydrogen Oxidation Reaction in Alkaline Electrolytes − A Review. *ACS Catal.* **2018**, *8* (7), 6665−6690.

(4) Dekel, D. R.; Amar, M.; Willdorf, S.; Kosa, M.; Dhara, S.; Diesendruck, C. E. Effect of Water on the Stability of Quaternary Ammonium Groups for Anion Exchange Membrane Fuel Cell Applications. *Chem. Mater.* **2017**, *29* (10), 4425−4431.

(5) Amel, A.; Smedley, S. B.; Dekel, D. R.; Hickner, M. A.; Ein-Eli, Y. Characterization and Chemical Stability of Anion Exchange Membranes Cross-Linked with Polar Electron-Donating Linkers. *J. Electrochem. Soc.* **2015**, *162* (9), F1047−F1055.

(6) Amel, A.; Gavish, N.; Zhu, L.; Dekel, D. R.; Hickner, M. A.; Ein-Eli, Y. Bicarbonate and chloride anion transport in anion exchange membranes. *J. Membr. Sci.* **2016**, *514*, 125−134.

(7) Pusara, S.; Srebnik, S.; Dekel, D. R. Molecular Simulation of Quaternary Ammonium Solutions at Low Hydration Levels. *J. Phys. Chem. C* **2018**, *122* (21), 11204−11213.

(8) Dekel, D. R.; Willdorf, S.; Ash, U.; Amar, M.; Pusara, S.; Dhara, S.; Srebnik, S.; Diesendruck, C. E. The critical relation between chemical stability of cations and water in anion exchange membrane fuel cells environment. *J. Power Sources* **2018**, *375*, 351−360.

(9) Gottesfeld, S.; Dekel, D. R.; Page, M.; Bae, C.; Yan, Y. S.; Zelenay, P.; Kim, Y. S. Anion exchange membrane fuel cells: Current status and remaining challenges. *J. Power Sources* **2018**, *375*, 170−184.

(10) Dekel, D. R. Review of cell performance in anion exchange membrane fuel cells. *J. Power Sources* **2018**, *375*, 158−169.

(11) Miller, H. A.; Vizza, V. Electrocatalysts and Mechanisms of Hydrogen Oxidation in Alkaline Media for Anion Exchange Membrane Fuel Cells. *Anion Exchange Membrane Fuel Cells: Principles, Materials and Systems. Lecture Notes in Energy* **2018**, *63*, 79−103.

(12) Durst, J.; Siebel, A.; Simon, C.; Hasche, F.; Herranz, J.; Gasteiger, H. A. New insights into the electrochemical hydrogen oxidation and evolution reaction mechanism. *Energy Environ. Sci.* **2014**, *7* (7), 2255−2260.

(13) Li, J.; Ghoshal, S.; Bates, M. K.; Miller, T. E.; Davies, V.; Stavitski, E.; Attenkofer, K.; Mukerjee, S.; Ma, Z. F.; Jia, Q. Experimental proof of the bifunctional mechanism for the hydrogen oxidation in alkaline media. *Angew. Chem., Int. Ed.* **2017**, *56* (49), 15594−155598.

(14) Schwämmlein, J. N.; El-Sayed, H. L.; Stühmeier, B. M.; Wagenbauer, K. F.; Dietz, H.; Gasteiger, H. A. Origin of Superior Activity of Ru@Pt Core-Shell Nanoparticles towards Hydrogen Oxidation in Alkaline Media. *ECS Trans.* **2016**, *75*, 971−982.

(15) Lu, S. Q.; Zhuang, Z. B. Investigating the Influences of the Adsorbed Species on Catalytic Activity for Hydrogen Oxidation Reaction in Alkaline Electrolyte. *J. Am. Chem. Soc.* **2017**, *139* (14), 5156−5163.

(16) Cong, Y. Y.; Yi, B. L.; Song, Y. J. Hydrogen oxidation reaction in alkaline media: From mechanism to recent electrocatalysts. *Nano Energy* **2018**, *44*, 288−303.

(17) Wang, T. Y.; Xie, H.; Chen, M. J.; D'Aloia, A.; Cho, J.; Wu, G.; Li, Q. Precious metal-free approach to hydrogen electrocatalysis for energy conversion: From mechanism understanding to catalyst design. *Nano Energy* **2017**, *42*, 69−89.

(18) Yang, F. L.; Fu, L. H.; Cheng, G. Z.; Chen, S. L.; Luo, W. Ir-oriented nanocrystalline assemblies with high activity for hydrogen oxidation/evolution reactions in an alkaline electrolyte. *J. Mater. Chem. A* **2017**, *5* (44), 22959−22963.

(19) Sheng, W. C.; Myint, M.; Chen, J. G. G.; Yan, Y. S. Correlating the hydrogen evolution reaction activity in alkaline electrolytes with the hydrogen binding energy on monometallic surfaces. *Energy Environ. Sci.* **2013**, *6* (5), 1509−1512.

(20) Henning, S.; Herranz, J.; Gasteiger, H. A. Bulk-Palladium and Palladium-on-Gold Electrocatalysts for the Oxidation of Hydrogen in Alkaline Electrolyte. *J. Electrochem. Soc.* **2015**, *162* (1), F178−F189.

(21) Wang, Y.; Wang, G. W.; Li, G. W.; Huang, B.; Pan, J.; Liu, Q.; Han, J. J.; Xiao, L.; Lu, J. T.; Zhuang, L. Pt-Ru catalyzed hydrogen oxidation in alkaline media: oxophilic effect or electronic effect? *Energy Environ. Sci.* **2015**, *8* (1), 177−181.

(22) Li, Q.; Peng, H.; Wang, Y.; Xiao, L.; Lu, J.; Zhuang, L. The Comparability of Pt to Pt-Ru in Catalyzing the Hydrogen Oxidation Reaction for Alkaline Polymer Electrolyte Fuel Cells Operated at 80 °C. *Angew. Chem., Int. Ed.* **2019**, *58* (5), 1442−1446.

(23) Strmcnik, D.; Uchimura, M.; Wang, C.; Subbaraman, R.; Danilovic, N.; van der Vliet, D.; Paulikas, A. P.; Stamenkovic, V. R.; Markovic, N. M. Improving the hydrogen oxidation reaction rate by promotion of hydroxyl adsorption. *Nat. Chem.* **2013**, *5* (4), 300−306.

(24) Miller, H. A.; Lavacchi, A.; Vizza, F.; Marelli, M.; Di Benedetto, F.; D'Acapito, F.; Paska, Y.; Page, M.; Dekel, D. R. A Pd/C-CeO2 Anode Catalyst for High-Performance Platinum-Free Anion Exchange Membrane Fuel Cells. *Angew. Chem. Int. Edit* **2016**, *55* (20), 6004−6007.

(25) Miller, H. A.; Vizza, F.; Marelli, M.; Zadick, A.; Dubau, L.; Chatenet, M.; Geiger, S.; Cherevko, S.; Doan, H.; Pavlicek, R. K.; Mukerjee, S.; Dekel, D. R. Highly active nanostructured palladium-ceria electrocatalysts for the hydrogen oxidation reaction in alkaline medium. *Nano Energy* **2017**, *33*, 293−305.

(26) Omasta, T. J. P.; Miller, H. A.; Vizza, F.; Wang, L.; Varcoe, J. R.; Dekel, D. R.; Mustain, W. E.; et al. Beyond 1.0 W cm-2 Performance Without Platinum − The Beginning of a New Era in Anion Exchange Membrane Fuel Cells. *J. Electrochem. Soc.* **2018**, *165* (15), J3039−J3044.

(27) Egorova, K. S.; Ananikov, V. P. Which Metals are Green for Catalysis? Comparison of the Toxicities of Ni, Cu, Fe, Pd, Pt, Rh, and Au Salts. *Angew. Chem., Int. Ed.* **2016**, *55* (40), 12150−12162.

(28) Yu, H.; Davydova, E. S.; Ash, U.; Miller, H. A.; Bonville, L.; Dekel, D. R.; Maric, R. Palladium-ceria nanocatalyst for hydrogen oxidation in alkaline media: Optimization of the Pd−CeO$_2$ interface. *Nano Energy* **2019**, *57*, 820−826.

(29) Cargnello, M.; Wieder, N. L.; Montini, T.; Gorte, R. J.; Fornasiero, P. Synthesis of Dispersible Pd@CeO2 Core-Shell Nanostructures by Self-Assembly. *J. Am. Chem. Soc.* **2010**, *132* (4), 1402−1409.

(30) Newville, M. IFEFFIT: interactive XAFS analysis and FEFF fitting. *J. Synchrotron Radiat.* **2001**, *8*, 322−324.

(31) Ravel, B.; Gallagher, K. Atomic structure and the magnetic properties of Zr-doped Sm2Co17. *Phys. Scr.* **2005**, *T115*, 606−608.

(32) Newville, M.; Livins, P.; Yacoby, Y.; Rehr, J. J.; Stern, E. A. Near-Edge X-Ray-Absorption Fine-Structure of Pb - a Comparison of Theory and Experiment. *Phys. Rev. B: Condens. Matter Mater. Phys.* **1993**, *47* (21), 14126−14131.

(33) Ankudinov, A. L.; Ravel, B.; Rehr, J. J.; Conradson, S. D. Real-space multiple-scattering calculation and interpretation of x-ray-absorption near-edge structure. *Phys. Rev. B: Condens. Matter Mater. Phys.* **1998**, *58* (12), 7565−7576.

(34) Wang, L.; Magliocca, E.; Cunningham, E. L.; Mustain, W. E.; Poynton, S. D.; Escudero-Cid, R.; Nasef, M. M.; Ponce-Gonzalez, J.; Bance-Souahli, R.; Slade, R. C. T.; Whelligan, D. K.; Varcoe, J. R. An optimized synthesis of high performance radiation-grafted anion-exchange membranes. *Green Chem.* **2017**, *19* (3), 831−843.

(35) Wang, L. Q.; Brink, J. J.; Liu, Y.; Herring, A. M.; Ponce-Gonzalez, J.; Whelligan, D. K.; Varcoe, J. R. Non-fluorinated pre-irradiation-grafted (peroxidated) LDPE-based anion-exchange membranes with high performance and stability. *Energy Environ. Sci.* **2017**, *10* (10), 2154−2167.

(36) Lu, Y. X.; Wang, L. Q.; Preuss, K.; Qiao, M.; Titirici, M. M.; Varcoe, J.; Cai, Q. Halloysite-derived nitrogen doped carbon electrocatalysts for anion exchange membrane fuel cells. *J. Power Sources* **2017**, *372*, 82−90.

(37) Wang, L. Q.; Bellini, M.; Miller, H. A.; Varcoe, J. R. A high conductivity ultrathin anion-exchange membrane with 500+h alkali stability for use in alkaline membrane fuel cells that can achieve 2 W cm(−2) at 80 degrees C. *J. Mater. Chem. A* **2018**, *6* (31), 15404−15412.

(38) Blum, V.; Gehrke, R.; Hanke, F.; Havu, P.; Havu, V.; Ren, X. G.; Reuter, K.; Scheffler, M. Ab initio molecular simulations with numeric atom-centered orbitals. *Comput. Phys. Commun.* **2009**, *180* (11), 2175−2196.

(39) Vanlenthe, E.; Baerends, E. J.; Snijders, J. G. Relativistic Total-Energy Using Regular Approximations. *J. Chem. Phys.* **1994**, *101* (11), 9783−9792.

(40) Perdew, J. P.; Burke, K.; Ernzerhof, M. Generalized gradient approximation made simple. *Phys. Rev. Lett.* **1996**, *77* (18), 3865−3868.

(41) Skulason, E.; Tripkovic, V.; Bjorketun, M. E.; Gudmundsdottir, S.; Karlberg, G.; Rossmeisl, J.; Bligaard, T.; Jonsson, H.; Norskov, J. K. Modeling the Electrochemical Hydrogen Oxidation and Evolution Reactions on the Basis of Density Functional Theory Calculations. *J. Phys. Chem. C* **2010**, *114* (42), 18182−18197.

(42) Johansson, M.; Skulason, E.; Nielsen, G.; Murphy, S.; Nielsen, R. M.; Chorkendorff, I. Hydrogen adsorption on palladium and palladium hydride at 1 bar. *Surf. Sci.* **2010**, *604* (7−8), 718−729.

(43) Amorim, C.; Keane, M. A. Palladium supported on structured and nonstructured carbon: A consideration of Pd particle size and the nature of reactive hydrogen. *J. Colloid Interface Sci.* **2008**, *322* (1), 196−208.

(44) Redjel, A.; Boudjahem, A.-G.; Bettahar, M. Effect of palladium precursor and preparation method on the catalytic performance of Pd/SiO2 catalysts for benzene hydrogenation. *Particulate Science and Technology* **2018**, *36*, 710−715.

(45) Konda, S. K.; Chen, A. C. Palladium based nanomaterials for enhanced hydrogen spillover and storage. *Mater. Today* **2016**, *19* (2), 100−108.

(46) Vayssilov, G. N.; Lykhach, Y.; Migani, A.; Staudt, T.; Petrova, G. P.; Tsud, N.; Skala, T.; Bruix, A.; Illas, F.; Prince, K. C.; Matolin, V.; Neyman, K. M.; Libuda, J. Support nanostructure boosts oxygen transfer to catalytically active platinum nanoparticles. *Nat. Mater.* **2011**, *10* (4), 310−315.

(47) Zhang, H. L.; Wang, J. L.; Zhang, Y. H.; Jiao, Y.; Ren, C. J.; Gong, M. C.; Chen, Y. Q. A study on H-2-TPR of Pt/Ce0.27Zr0.73O2 and Pt/Ce0.27Zr0.70La0.03Ox for soot oxidation. *Appl. Surf. Sci.* **2016**, *377*, 48−55.

(48) Dutta, G.; Waghmare, U. V.; Baidya, T.; Hegde, M. S. Hydrogen spillover on CeO2/Pt: Enhanced storage of active hydrogen. *Chem. Mater.* **2007**, *19* (26), 6430−6436.

(49) Yan, Z.; Tomer, A.; Perrussel, G.; Ousmane, M.; Katryniok, B.; Dumeignil, F.; Ponchel, A.; Liebens, A.; Pera-Titus, M. A Pd/CeO2 "H-2 Pump" for the Direct Amination of Alcohols. *ChemCatChem* **2016**, *8* (21), 3347−3352.

(50) Loglio, F.; Innocenti, M.; D'Acapito, F.; Felici, R.; Pezzatini, G.; Salvietti, E.; Foresti, M. L. Cadmium selenide electrodeposited by ECALE: electrochemical characterization and preliminary results by EXAFS. *J. Electroanal. Chem.* **2005**, *575* (1), 161−167.

(51) Krishnankutty, N.; Vannice, M. A. The Effect of Pretreatment on Pd/C Catalysts 0.1. Adsorption and Absorption Properties. *J. Catal.* **1995**, *155* (2), 312−326.

(52) Song, W. Y.; Su, Y. Q.; Hensen, E. J. M. A DFT Study of CO Oxidation at the Pd-CeO2(110) Interface. *J. Phys. Chem. C* **2015**, *119* (49), 27505−27511.

(53) Li, W. Q.; Goverapet Srinivasan, S.; Salahub, D. R.; Heine, T. Ni on the CeO2(110) and (100) surfaces: adsorption vs. substitution effects on the electronic and geometric structures and oxygen vacancies. *Phys. Chem. Chem. Phys.* **2016**, *18* (16), 11139−11149.

(54) Skulason, E.; Tripkovic, V.; Bjorketun, M. E.; Gudmundsdottir, S.; Karlberg, G.; Rossmeisl, J.; Bligaard, T.; Jonsson, H.; Norskov, J. K. Modeling the Electrochemical Hydrogen Oxidation and Evolution Reactions on the Basis of Density Functional Theory Calculations (vol 114, pg 18182, 2010). *J. Phys. Chem. C* **2010**, *114* (50), 22374−22374.

(55) Zheng, J.; Nash, J.; Xu, B.; Yan, Y. Perspective—Towards Establishing Apparent Hydrogen Binding Energy as the Descriptor for Hydrogen Oxidation/Evolution Reactions. *J. Electrochem. Soc.* **2018**, *165* (2), H27−H29.

(56) Ponce-Gonzalez, J.; Ouachan, I.; Varcoe, J. R.; Whelligan, D. K. Radiation-induced grafting of a butyl-spacer styrenic monomer onto ETFE: the synthesis of the most alkali stable radiation-grafted anion-exchange membrane to date. *J. Mater. Chem. A* **2018**, *6* (3), 823−827.

(57) Omasta, T. J.; Wang, L.; Peng, X.; Lewis, C. A.; Varcoe, J. R.; Mustain, W. E. Importance of balancing membrane and electrode water in anion exchange membrane fuel cells. *J. Power Sources* **2018**, *375*, 205−213.

(58) Wang, L. Q.; Brink, J. J.; Varcoe, J. R. The first anion-exchange membrane fuel cell to exceed 1 W cm(−2) at 70 degrees C with a non-Pt-group (O-2) cathode. *Chem. Commun.* **2017**, *53* (86), 11771−11773.